Processing and Application of Ceramics 14 [2] (2020) 102–112
https://doi.org/10.2298/PAC2002102D

Influence of oxygen vacancy defects and cobalt doping on optical, electronic and photocatalytic properties of ultrafine $SnO_{2-\delta}$ nanocrystals

Zorana D. Dohčević-Mitrović[1,*], Vinicius D. Araújo[2], Marko Radović[3], Sonja Aškrabić[1], Guilherme R. Costa[4], Maria Ines B. Bernardi[4], Dejan M. Djokić[1], Bojan Stojadinović[1], Marko G. Nikolić[5]

[1]*Nanostructured Matter Laboratory, Institute of Physics Belgrade, University of Belgrade, Pregrevica 118, 11080 Belgrade, Serbia*
[2]*NanoA-UACSA, Universidade Federal Rural de Pernambuco, UFRPE, Cabo de Santo Agostinho, PE, Brazil*
[3]*University of Novi Sad, Group for Nano and Microelectronics, Biosense Institute, Novi Sad, Serbia*
[4]*Instituto de Física de São Carlos, Universidade de São Paulo, USP, 13560-970, São Carlos – SP, Brasil*
[5]*Institute of Physics Belgrade, University of Belgrade, P.O. Box 68, Pregrevica 118, 11080 Belgrade, Serbia*

Received 12 November 2019; Received in revised form 21 February 2020; Accepted 15 March 2020

Abstract

Ultrafine pure and cobalt doped $SnO_{2-\delta}$ nanocrystals ($Sn_{1-x}Co_xO_{2-\delta}$, $0 \leq x \leq 0.05$) were synthesized by microwave-assisted hydrothermal method. The as-prepared nanocrystals have single phase tetragonal rutile structure. With increase of Co content ($x > 0.01$), Co entered into SnO_2 lattice in mixed Co^{2+}/Co^{3+} state. Pronounced blue shift of the band gap with cobalt doping originated from the combined effect of quantum confinement and Burnstain-Moss shift. Raman and photoluminescence study revealed oxygen deficient structure of $SnO_{2-\delta}$ for which the prevalent defects are in the form of in-plane oxygen vacancies. Co-doping induced decrease of in-plane oxygen vacancy concentration and luminescence quenching. $SnO_{2-\delta}$ exhibited significantly better photocatalytic activity under UV light irradiation, than Co-doped samples due to better UV light absorption and increased concentration of in-plane oxygen vacancies which, as shallow donors, enable better electron-hole separation and faster charge transport.

Keywords: *SnO_2 nanopowders, wet-chemical synthesis, defects, optical properties, photocatalysis*

I. Introduction

Tin oxide (SnO_2) is an n-type semiconductor with large band gap (3.6 eV) at room temperature. Because of its unique electronic, optical and electrochemical properties, SnO_2 is widely used in dye-sensitized solar cells, transparent conductive electrodes, solid state sensors, lithium-ion batteries and catalysis [1–7]. During the past decade, SnO_2 nanostructures have become one of the most important oxide nanostructures due to their exceptional properties and potential applications which are strongly influenced by size effects and morphology [8].

In the past decade various efforts were devoted to the synthesis of SnO_2 nanostructures with controlled size and morphology. SnO_2 nanostructures like thin films, nanobelts, nanotubes or nanowires, nanodisks and nanocrystals have been prepared using different methods, such as carbothermal reduction process, hydrothermal and solvothermal, chemical vapour condensation, laser ablation, sol-gel and molten salt techniques [9–18]. However, for most of these methods relatively high temperatures are required during the synthesis process and the samples are usually subjected to additional thermal treatment in order to achieve good crystallinity. In recent years hydrothermal approaches appeared to be widely applied as SnO_2 nanostructures can be obtained with different morphologies and tunable size at mild temperatures [8,19]. Microwave-assisted hydrothermal

*Corresponding author: tel: +381 113713024,
e-mail: *zordoh@ipb.ac.rs*

synthesis (MAH) became a very promising method for obtaining size and morphology controllable oxide nanostructures due to the unique advantages, such as fast heating rate and uniform heating without superheating of the solvent, which results in small particle size, narrow size distribution and high purity of the obtained nanopowders. Therefore, MAH appeared to be very convenient method for obtaining ultrafine SnO_2 nanopowders [19,20].

SnO_2 nanostructures are generally less studied as potential photocatalysts compared to TiO_2 and ZnO, despite its crystalline structure being similar to TiO_2 and good properties such as high photochemical stability, non-toxic nature, strong oxidizing power, and low-cost [21]. In order to improve the photocatalytic efficiency of SnO2, selective doping with metal ions, transition metals (gold, manganese, silver and iron) and rare–earth elements (Ce, Sm, Gd) was performed and well presented in the review paper by Al-Hamdi *et al.* [21]. Among the transition metals, cobalt is rarely applied as dopant. In fact, there are only few papers dedicated to potential applicability of Co-doped SnO_2 nanostructures as photocatalysts [22–24], but none of them investigated the synergic influence of defective nature and Co-doping on photocatalytic properties of very fine SnO_2 nanocrystals. It is well known that photocatalytic efficiency of metal oxide nanostructures can be influenced by the presence of intrinsic defects such as oxygen vacancies [25–28]. The presence of oxygen vacancies strongly influences the charge recombination process and the band gap structure. Namely, oxygen vacancies introduce the defect levels (near conduction or valence band) inside the gap and behave as trapping centres for photogenerated carriers preventing the fast recombination. Besides, oxygen vacancies can facilitate the transferring of charge carriers to adsorbed species (OH^- or water molecules and dissolved oxygen present on the surface of the catalyst) and enhance the formation of reactive radicals which are responsible for improved photocatalytic activity of oxide nanostructures [26,27]. Moreover, the formation of defect states inside the gap reduces the band gap and extends the absorption to visible light [25,27]. The prominent intrinsic defects in SnO_2 nanostructures are oxygen vacancies as well, which form donor/acceptor states inside the SnO_2 gap, influencing its electronic structure and making it conductive [4]. As oxygen vacancies play a critical role in many new physical phenomena, it is important to investigate associated changes in the optical and electronic properties of pure and Co-doped SnO_2 nanomaterials which can have a strong impact on photocatalytic activity of these materials.

In the work presented here, ultrafine, nonstoichiometric pristine and Co-doped $SnO_{2-\delta}$ nanopowders were synthesized via simple and cost effective microwave-assisted hydrothermal method. This paper intends to explore how defective structure and Co-doping provoke changes of optical and electronic properties of $SnO_{2-\delta}$ nanocrystals influencing the photocatalytic performances.

II. Experimental procedure

2.1. Materials preparation

$Sn_{1-x}Co_xO_{2-\delta}$ (where x = 0, 1, 3 and 5 mol%) nanopowders were synthesized by microwave-assisted hydrothermal method using $SnCl_4 \cdot 5\,H_2O$ (98%, Aldrich), $CoCl_2 \cdot 6\,H_2O$, NaOH and HCl as starting precursors. Initially, 1 ml of hydrochloric acid was added to 10 ml of distilled water at 50 °C resulting in a solution with pH between 0 and 1. Next, 17.529 g of $SnCl_4 \cdot 5\,H_2O$ was added and the mixed solution was homogenized under stirring with simultaneous increasing of the water amount to approximately 50 ml. In a case of the doped samples, 0.119 g, 0.357 g and 0.595 g of $CoCl_2 \cdot 6\,H_2O$ were added to obtain 1, 3 and 5 mol% Co-doped samples, respectively. NaOH was added dropwise under vigorous stirring until the pH of the solution was adjusted to 8. The mixed solution was placed in a 110 ml sealed Teflon autoclave and subjected to microwave heating, applying 2.45 GHz of microwave radiation at a maximum power of 800 W. The as-prepared solution was heated at 140 °C for 10 min using heating rate of 14 °C/min and then air-cooled to room temperature. The as-prepared undoped and Co-doped $SnO_{2-\delta}$ nanopowders were submitted to dialysis in order to be separated from the solution and then dried at 80 °C for 12 h.

2.2. Materials characterization

The crystalline structure and average crystallite size of the $Sn_{1-x}Co_xO_{2-\delta}$ samples were evaluated using X-ray diffraction (XRD) measurements. The measurements were carried out using an automatic X-ray diffractometer (Rigaku, Rotaflex RU200B) with CuKα radiation (50 kV, 100 mA, λ = 1.5405 Å) in a θ–2θ configuration using a graphite monochromator. The 2θ scanning range was between 20 and 70°, with a step size of 0.02°. Microstructural analysis was made by transmission electron microscopy (TEM) FEI Titan 60-300 operating at voltages between 60 and 300 kV, using a field emission gun (FEG) with an objective lens (Super Twin) and a corrector that allows resolution of 0.08 nm.

Micro-Raman scattering measurements were performed at room temperature in the backscattering configuration on Tri Vista 557 Raman system equipped with a nitrogen-cooled CCD detector, using 532 nm laser line of optically pumped semiconductor laser (Coherent Verdi G) as an excitation source. UV-visible diffuse reflectance spectra were acquired with a Cary 5G spectrophotometer in the 200–800 nm range. Diffuse reflectance spectra were transformed into the absorbance spectra by the Kubelka-Munk method. The ellipsometric measurements were performed using high resolution variable angle spectroscopic ellipsometer (SOPRA GES5E-IRSE) of the rotating polarizer type. The data

were collected at room temperature in the UV-Vis spectral range with a resolution of 0.02 eV, for the incidence angle of 70°. Photoluminescence emission measurements were performed at room temperature using Spex Fluorolog spectrofluorometer with C31034 cooled photomultiplier under Xenon lamp excitation at 380 nm.

2.3. Photocatalytic experiments

The photocatalytic activity of the $Sn_{1-x}Co_xO_{2-\delta}$ samples, for the degradation of methylene blue (MB) as model pollutant, was tested under UV illumination. The different samples with the same photocatalyst amount (150 mg/l) were immersed in 20 ml of an aqueous solution of methylene blue (5.0 mg/l). The beakers were placed in a photo-reactor at controlled temperature (15 °C), under magnetic stirring, and were illuminated by six 15 W UV lamps (TUV Philips, maximum intensity at 254 nm). The solution was placed in the dark for 60 min to reach the adsorption/desorption equilibrium before UV light exposure. Blank experiment without UV irradiation demonstrated no adsorption of MB dye on the surface of the $Sn_{1-x}Co_xO_{2-\delta}$ samples. The photocatalytic experiments were conducted at the natural pH = 6 of MB dye. At regular time intervals 2 ml aliquots were taken, centrifuged to remove any catalyst particles and the concentration of the dye was determined by UV-Vis absorption spectrophotometer (Shimadzu-UV-1601 PC) monitoring the variation of absorbance at 663 nm.

The formation of hydroxyl radicals ($OH^{\bullet}$) on the surface of the $SnO_{2-\delta}$ sample under the UV light illumination was examined by photoluminescence (PL) technique using terephthalic acid (TA) as a probe molecule. The detailed experimental procedure was described in reference [29]. TA is known to react with $OH^{\bullet}$ radicals induced on the photocatalyst's surface where it produces highly fluorescent 2-hydroxyterephthalic acid which shows an intense PL peak at around 425 nm. The intensity of this peak is proportional to the amount of $OH^{\bullet}$ radicals [30,31] produced in the photocatalytic process. The changes of the 425 nm PL peak intensity were measured at room temperature using 315 nm excitation.

III. Results and discussion

3.1. Crystal structure and morphology

Figure 1a shows XRD patterns of the $Sn_{1-x}Co_xO_{2-\delta}$ ($0 \le x \le 0.05$) nanopowders, whereas the Rietveld refined XRD spectra of the $SnO_{2-\delta}$ and $Sn_{0.95}Co_{0.05}O_{2-\delta}$ samples are presented in Figs. 1b and 1c. The XRD patterns of all the samples revealed single phase tetragonal structure (cassiterite phase). The XRD peaks at 26.6, 33.8, 51.9 and 65.8° can be assigned to (110), (101), (211) and (301) planes, which are in good agreement with literature data (ICDS № 9163). No secondary phases like Co oxides, Co clusters or other tin oxide phases were observed. Moreover, broad diffraction peaks of low intensities compared to those of bulk SnO_2, point to low crystallinity and small crystallite size of the SnO_2 nanoparticles.

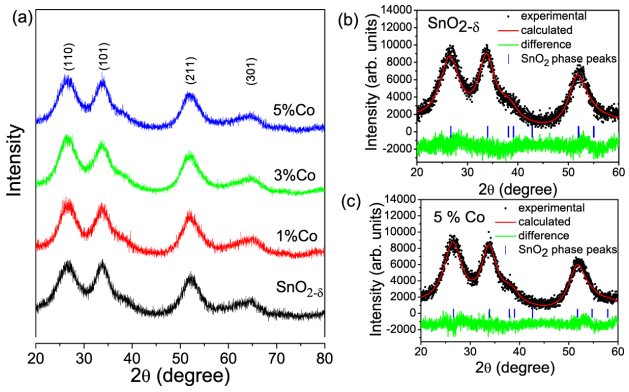

Figure 1. XRD patterns of $Sn_{1-x}Co_xO_{2-\delta}$ nanocrystals ($0 \le x \le 0.05$) indexed to tetragonal rutile structure of SnO_2 (a), Rietveld refined XRD spectra of $SnO_{2-\delta}$ (b) and $Sn_{0.95}Co_{0.05}O_{2-\delta}$ (c) nanoparticles

The average lattice parameters and unit cell volume obtained from the Rietveld refinement data are given in Table 1. These results showed an expansion of the SnO_2 unit cell with increasing cobalt content up to 5%. This variation originates from the substitution of smaller Sn^{4+} cations (0.83 Å) with larger Co^{2+} cations in high spin state (0.89 Å) [32]. The slight shrinkage of the unit cell observed for the 5% Co-doped sample can be related to the presence of increased amount of smaller Co^{3+} cations (*ls*: 0.68 Å or *hs*: 0.75 Å). The average crystallite size (D) of the $Sn_{1-x}Co_xO_{2-\delta}$ nanocrystals was calculated with the Scherrer formula using the 110 reflection and their values are reported in Table 1. Obviously, the mean crystallite sizes of the undoped and Co-doped samples are less than Bohr exciton radius (2.7 nm for SnO_2) [33] and with increased Co-doping the crystallite size of the $Sn_{1-x}Co_xO_{2-\delta}$ nanocrystals decreases. Such a trend implies that Co-doping has an inhibiting effect on the crystal growth. This inhibiting effect of Co on the crystal grains growth was already confirmed in the work of Babu *et al.* [34].

TEM images of the undoped and Co-doped $SnO_{2-\delta}$ samples are presented in Fig. 2. TEM images revealed

Table 1. Lattice parameters (a, c), unit cell volume (V) and average crystallite size (D) of the $Sn_{1-x}Co_xO_{2-\delta}$ nanocrystals

Sample	$a = b$ [Å]	c [Å]	V [Å^3]	D [nm]
$SnO_{2-\delta}$	4.722 ± 0.002	3.180 ± 0.003	70.905	2.5
$Sn_{0.99}Co_{0.01}O_{2-\delta}$	4.747 ± 0.002	3.201 ± 0.003	72.131	2.4
$Sn_{0.97}Co_{0.03}O_{2-\delta}$	4.759 ± 0.002	3.206 ± 0.002	72.609	2.3
$Sn_{0.95}Co_{0.05}O_{2-\delta}$	4.744 ± 0.002	3.186 ± 0.002	71.703	2.2

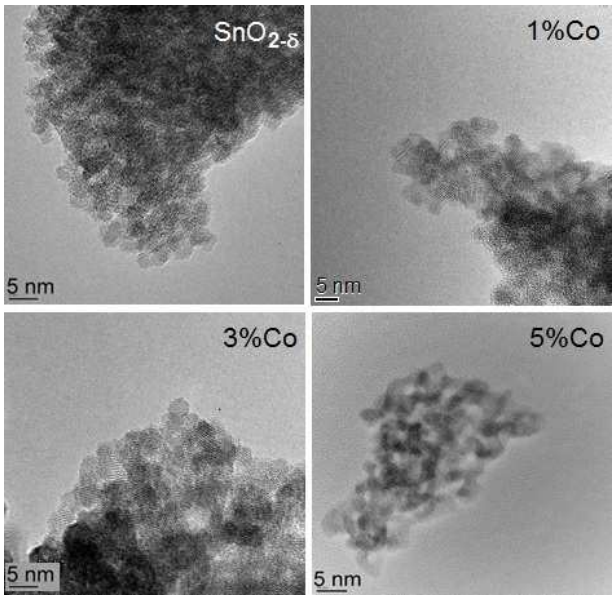

Figure 2. TEM images of $Sn_{1-x}Co_xO_{2-\delta}$ ($0 \le x \le 0.05$) nanoparticles

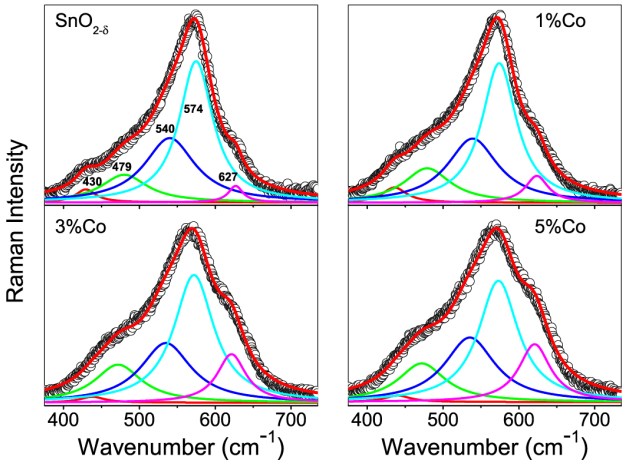

Figure 3. Deconvoluted room-temperature Raman spectra of $Sn_{1-x}Co_xO_{2-\delta}$ nanoparticles

that the undoped $SnO_{2-\delta}$ sample is composed of single crystalline nanoparticles of very small size and quasi-spherical shape. The morphology of the $Sn_{1-x}Co_xO_{2-\delta}$ nanoparticles remained the same with Co-doping. The particles are of spherical shape with the size less than 3 nm, which is in good agreement with the results obtained from XRD data. The observed agglomeration of the $Sn_{1-x}Co_xO_{2-\delta}$ nanoparticles can be ascribed to small crystallite sizes.

3.2. Raman analysis

SnO_2 tetragonal rutile crystalline structure (space group $P4_2/mnm$) has four active Raman modes (non-degenerate A_{1g}, B_{1g}, B_{2g} modes, and a doubly degenerated E_g mode), two active infrared modes (A_{2u} and E_u) and two silent modes (A_{2g}, B_{1u}) [35]. The positions of A_{1g}, B_{1g}, B_{2g} and E_g Raman modes in SnO_2 single crystal under ambient conditions are 634, 123, 776 and 475 cm^{-1}, respectively, and the A_{1g} and E_g modes are of much higher intensity compared to B_{1g} and B_{2g} modes [35].

The Raman spectra of nanocrystalline, non-stoichiometric $SnO_{2-\delta}$ are modified in comparison with single-crystal or polycrystalline SnO_2, because Raman spectroscopy is more sensitive to intrinsic defects and confinement effect than conventional XRD technique. Namely, the position, bandwidth and intensity of Raman modes are size dependent, i.e. Raman modes are broadened, of lower intensity and shifted towards lower or higher energies depending on phonon dispersion curves. Besides, new modes of defect origin can appear [36,37]. The room temperature Raman spectra of the $Sn_{1-x}Co_xO_{2-\delta}$ nanocrystals are presented in Fig. 3 and they are deconvoluted using Lorentzian profiles (full lines in Fig. 3).

In the Raman spectrum of the pure $SnO_{2-\delta}$, the most prominent mode is located at ~574 cm^{-1}. This mode is characteristic for non-stoichiometric $SnO_{2-\delta}$ and it is not present in the Raman spectra of SnO_2 single-crystal [35]. Density functional calculations performed by Liu *et al.* [38] have shown that this mode arises from in-plane oxygen vacancies (V_{Oin}) in the surface region of $SnO_{2-\delta}$ nanoparticles, intensity of which is proportional to their concentration. In very fine nanoparticles this mode has the highest intensity due to the increased concentration of oxygen vacancies. Raman mode at ~627 cm^{-1} can be ascribed to the A_{1g} mode of rutile SnO_2 structure. This mode is of lower intensity, broadened and shifted to lower wave numbers compared to the bulk counterpart, due to the phonon confinement effect [37]. As the crystallite size of the undoped $SnO_{2-\delta}$ is smaller than the Bohr exciton radius, the size effect can be very pronounced in this sample. Another broad Raman mode at ~479 cm^{-1} is assigned to E_g mode and it is shifted to higher wavenumbers with size decrease of $SnO_{2-\delta}$ nanocrystals [37]. Besides these modes, additional modes at around 430 and 540 cm^{-1} appear. These new modes are usually seen in very fine SnO_2 nanoparticles [37–39], nanotubes [40] or nanoribbons [41] because of the increased degree of local disorder, i.e. loss in long-range order due to the large number of lattice vacant positions, especially at the surface of nanoparticles. These modes are of high intensity in small nanoparticles and disappear with particle size increase. According to some literature data, due to the relaxation of the selection rules in nanostructured SnO_2, the mode at 540 cm^{-1} is assigned to the Raman forbidden mode (B_{1u}) [40,41], whereas the new mode at around 430 cm^{-1} can be assigned to the oxygen vacancy clusters (V_C) [39]. The A_{1g} and E_g modes exhibited redshift and broadening with Co-doping. The redshift and broadening of these modes are expected with substitution of Sn^{4+} ions with larger Co^{2+} ions and decreased crystallite size due to the phonon confinement effect. The positions and intensities of the A_{1g}, E_g and oxygen vacancy related modes (V_{Oin} and V_C) are presented in Fig. 4. As it can be seen from Fig. 4, the intensity of A_{1g} mode increases with increased Co concentration, whereas the intensity of E_g

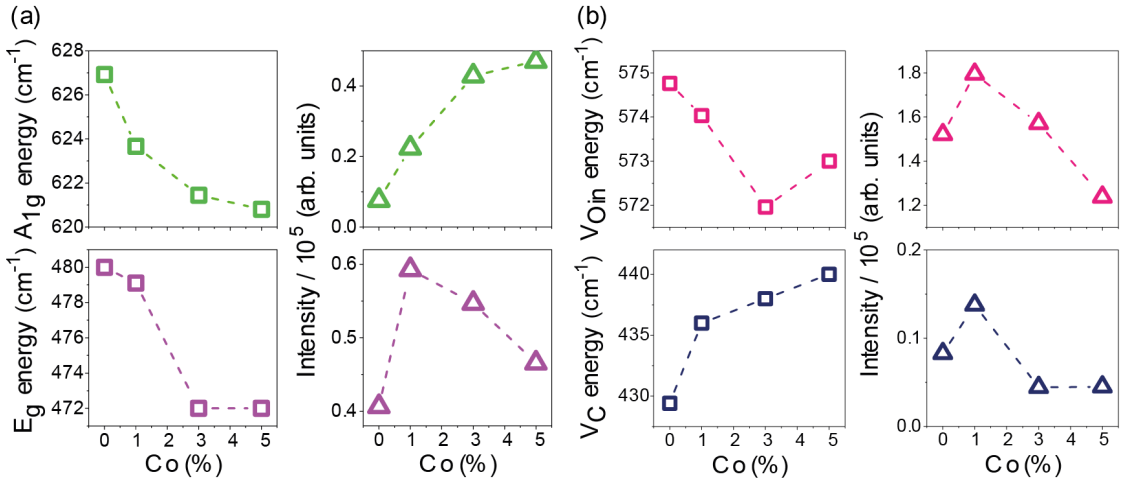

Figure 4. Positions and intensities of A_{1g} and E_g (a) and vacancy (V_{Oin} and V_C) (b) Raman modes

mode is higher in the Co-doped samples compared to the undoped $SnO_{2-\delta}$. The E_g mode intensity slightly decreased in samples doped with higher Co content, as a consequence of lattice distortion and reduction in lattice space symmetry. The position of the Raman mode ascribed to in-plane oxygen vacancies (574 cm^{-1}) did not change significantly, whereas the Raman mode related to vacancy clusters (430 cm^{-1}) shifts to higher energies with Co-doping. The intensity of both modes decreased in the $Sn_{0.97}Co_{0.03}O_{2-\delta}$ sample and this trend is more evident for the $Sn_{0.95}Co_{0.05}O_{2-\delta}$ sample. The intensity reduction of oxygen vacancy related modes in these samples implies that the concentration of oxygen vacancies decreased. The decrease of the oxygen vacancy concentration is expected if the part of Co cations were in Co^{3+} state or if some Co cations were interstitially incorporated in $SnO_{2-\delta}$ lattice [33,42].

In order to see if Co cations substituted Sn^{4+} in Co^{2+} state or the part of them was in Co^{3+} state, UV-Vis absorption measurements were performed and the absorption spectra of the $Sn_{1-x}Co_xO_{2-\delta}$ samples are presented in Fig. 5. In the UV range, the absorption spectrum of $SnO_{2-\delta}$ displays a strong absorption due to

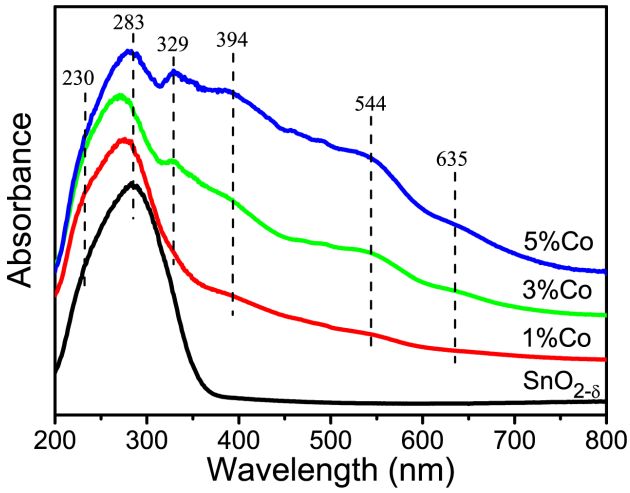

Figure 5. UV-Vis spectra of $Sn_{1-x}Co_xO_{2-\delta}$ nanoparticles

the SnO_2 interband transition. Two peaks at 230 and 283 nm are superimposed giving the broad band which might correspond to the surface Sn^{4+} species and to the $Sn^{4+} \rightarrow Sn^{2+}$ intervalence charge transfer, respectively [43]. In Co-doped samples the broad band is shifted to lower wavelength implying the band gap increase with Co-doping. In the absorption spectra of the $Sn_{0.97}Co_{0.03}O_{2-\delta}$ and $Sn_{0.95}Co_{0.05}O_{2-\delta}$ samples, new bands appear. The band around 329 nm can be assigned to the partial change of oxidation state of Co^{2+} to Co^{3+} [44], whereas the broad band around 400 nm can be ascribed to $^1A_{1g} \xrightarrow{\nu_2} {}^1T_{2g}$ transition of low spin Co^{3+} ions in octahedral environment [45]. The intensity of these bands increased in the $Sn_{0.95}Co_{0.05}O_{2-\delta}$ sample pointing to the increased concentration of Co^{3+} ions. The bands around 544 and 635 nm can be related to $^4A_2(F) \xrightarrow{\nu_2} {}^4T_1(P)$ transition of tetrahedral Co^{2+} species [45]. Therefore, from the absorption spectra of the $Sn_{0.97}Co_{0.03}O_{2-\delta}$ and $Sn_{0.95}Co_{0.05}O_{2-\delta}$ samples it can be deduced that part of Co cations entered into SnO_2 lattice in Co^{3+} state, concentration of which increased with the increased dopant content. This result supports the finding obtained from the refined XRD spectrum of the $Sn_{0.95}Co_{0.05}O_{2-\delta}$ sample, since the shrinkage of the unit cell was ascribed to the increased amount of Co^{3+} cations.

Our conclusions derived from absorption measurements are well-supported by recently published work of Roy *et al.* [46] concerning Co-doped SnO_2 nanocrystals. From the XPS study, Roy *et al.* [46] confirmed the mixed valence nature of Co ions in the host lattice and they have found that the relative concentration of Co^{3+} exceeds that of Co^{2+} with the increase of dopant content. This study also showed that Co incorporation into SnO_2 leads to the reduction of oxygen vacancies which is consistent with our Raman study.

3.3. Optical and electronic properties

The investigation of complex dielectric function by spectroscopic ellipsometry offers an insight into the

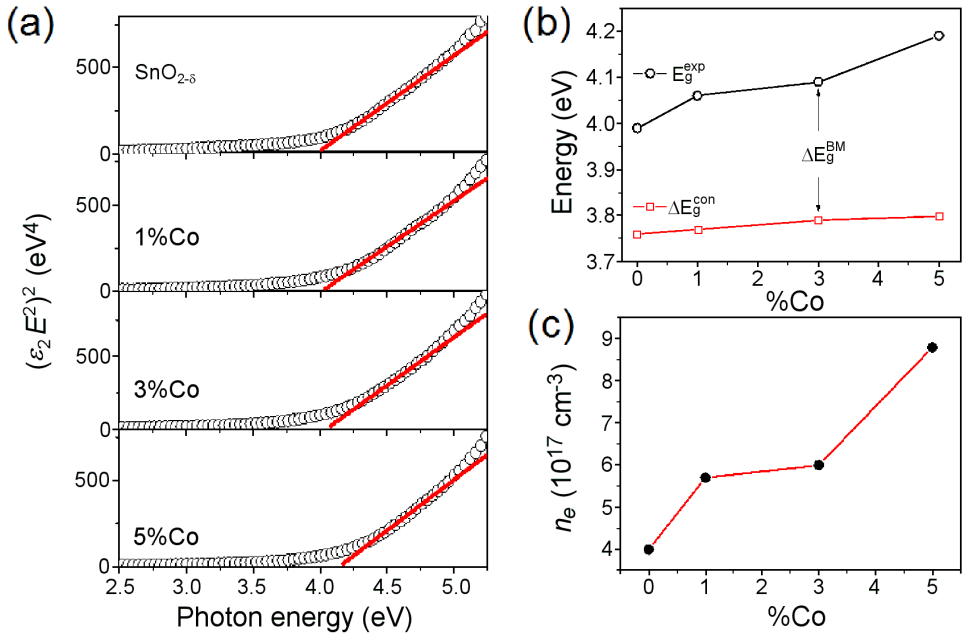

Figure 6. Determination of the direct band gap for $Sn_{1-x}Co_xO_{2-\delta}$ nanoparticles using Tauc law(a); variation of the band gap energy obtained from ellipsometric measurements (E_g^{exp}) and from quantum confinement model (ΔE_g^{con}) (b) and concentration of charge carriers n_e for $Sn_{1-x}Co_xO_{2-\delta}$ samples (c)

most important optical properties of the nanomaterials, such as, optical band gap, interband and intraband transitions, defect electronic states. The imaginary part of dielectric function is directly related to the electronic density of states and in a case of nanopowders it can be deduced from the ellipsometric measurements by applying two-phase model approximation (in our case: $SnO_{2-\delta}$ nanocrystals/air). In order to investigate the optical band gap behaviour and the influence of Co dopant on the absorption edge in $SnO_{2-\delta}$ nanocrystals we applied the Tauc model for direct band gap transition [47], knowing that SnO_2 is a direct band gap material [48]. In this case general expression for $\varepsilon_2(E)$ is:

$$(\varepsilon_2 \cdot E^2)^2 = a(E - E_g) \tag{1}$$

where E is the photon energy, E_g is the band gap and a is the constant related to the density of states for the conduction band. The Tauc plots of the $Sn_{1-x}Co_xO_{2-\delta}$ samples obtained from ellipsometric measurements are presented in Fig. 6a. Linear extrapolation to zero absorption (straight lines in Fig. 6a) gives the band gap energy values of the $Sn_{1-x}Co_xO_{2-\delta}$ samples.

In Fig. 6b, the dependence of the band gap energy (from Fig. 6a) on dopant content for the $Sn_{1-x}Co_xO_{2-\delta}$ samples is represented with open circles. It is obvious that Co-doping induces an increase of the E_g. Also, it is important to notice that all investigated samples have the band gap values higher than that for bulk SnO_2. Such changes in electronic properties of SnO_2 nanomaterials can be a consequence of the quantum confinement effect. This effect causes an increase of the band gap value due to the stronger localization of electronic states inside the volume of nanocrystals. The band gap energy shift, caused by this effect, can be calculated according to the following relation [49]:

$$\Delta E_g^{con} = E_g + \frac{\hbar^2 \pi^2}{2\mu \cdot D^2} \tag{2}$$

where E_g is the band gap value for the bulk SnO_2 (3.6 eV), D is the crystallite radius and μ is the reduced effective mass of the electron-hole pair. From the XRD results it was obtained that the average crystallite size of the undoped $SnO_{2-\delta}$ nanocrystals is lower than Bohr exciton radius, and that it has a tendency of further decrease with Co-doping. Therefore, it is reasonable to take into account the quantum confinement effect in order to properly analyse the band gap behaviour of the $Sn_{1-x}Co_xO_{2-\delta}$ samples. Taking the D values from Table 1 and knowing that $\mu = 0.38m_0$ [48], the band gap values (ΔE_g^{con}) that arise from the quantum confinement effect were calculated using Eq. 2. The ΔE_g^{con} values are presented in Fig. 6b with open squares. Comparing the ΔE_g^{con} values with E_g^{exp} ones it is obvious that observed band gap increase of the $Sn_{1-x}Co_xO_{2-\delta}$ samples cannot be ascribed only to the quantum confinement effect.

Another effect that can cause a shift of optical absorption edge to higher energies is the Burstein-Moss effect, which becomes more relevant in doped semiconductors (like transparent conducting oxides) with high charge carrier concentration. The Burstein-Moss effect is already registered in doped SnO_2 thin films [50,51]. According to this effect, the widening of the optical gap is caused by metallic doping and increase of carrier density which leads to the filling of empty semiconductor electronic states in the vicinity of Fermi level and its shift to higher energies. Assuming parabolic bands and

spherical Fermi surface the band gap shift due to the Burstein-Moss effect can be calculated by simple relation [4]:

$$\Delta E_g^{BM} = \frac{h^2}{2\mu}\left(3\pi^2 \cdot n_e\right)^{2/3} \quad (3)$$

where h is Planck constant, μ is the reduced effective mass and n_e is the carrier concentration.

Additional charge, i.e. increased charge carrier density in pure and doped $SnO_{2-\delta}$ nanocrystals, can originate from the donor type defects like oxygen vacancies and Co-dopants. Raman spectra have already evidenced defective structure of $SnO_{2-\delta}$, whereas Co^{2+} dopants bring additional charge when substituting Sn^{4+} ions. Hence, the observed increase of the E_g from Fig. 6b can be ascribed to the Burstein-Moss shift (ΔE_g^{BM}). Combining Eqs. 2 and 3 it is possible to estimate the concentration of charge carriers (n_e) in the $Sn_{1-x}Co_xO_{2-\delta}$ samples and the obtained values are presented in Fig. 6c. These calculated values are in good agreement with literature data for SnO_2 thin films [52]. As can be seen from Fig. 6c, doping of $SnO_{2-\delta}$ nanocrystals with Co ions causes an increase of the charge carriers concentration and shift of the optical absorption edge toward UV region, making the investigated material more conductive and at the same time more transparent.

It is well known that large number of defects, such as oxygen vacancies or vacancy clusters, can be formed at the SnO_2 nanoparticles surface and subsurface [21]. Intrinsic oxygen vacancies can be of three types: in-plane (V_{Oin}), bridging (V_{OB}) and subbridging (V_{OSB}) vacancies [36,38]. These vacancies can be in different charge states, i.e. vacancies which trap one, two or none electrons, so called F^+, F^0 and F^{++} centres, and they can form defect levels inside the $SnO_{2-\delta}$ gap [53]. Among the optical spectroscopy methods, photoluminescence (PL) spectroscopy is convenient method to investigate the defect structure of the pure and Co-doped $SnO_{2-\delta}$ samples.

Room temperature PL spectra of the $SnO_{2-\delta}$, $Sn_{0.99}Co_{0.01}O_{2-\delta}$ and $Sn_{0.95}Co_{0.05}O_{2-\delta}$ samples using a wavelength of 380 nm for excitation are presented in Fig. 7a. The PL spectrum of $SnO_{2-\delta}$ is deconvoluted into four Gaussian peaks centred at 510, 575, 470 and 446 nm (inset of Fig. 7a). In the deconvoluted PL spectrum of the undoped $SnO_{2-\delta}$ two bands dominate: broad intense band centred at around 510 nm and another band of lower intensity at around 575 nm. Since the excitation and emissions are both lower than the band gap of $SnO_{2-\delta}$, neither of these PL bands can be ascribed to the recombination of the Sn $4p$ conduction electrons with a holes from a O $2p$ band. The broad green luminescence around 510 nm is already seen in SnO_2 thin films [10] and nanoparticles [36] and it was attributed to the in-plane oxygen vacancy defects [36]. Therefore, the strong PL peak at 510 nm (2.45 eV) is ascribed to V_{Oin} defects. This finding is in accordance with corresponding Raman spectrum in which the most prominent Raman mode originates from in-plane oxygen vacancies. Another PL band at 575 nm (2.15 eV) can be ascribed to the isolated bridging oxygen vacancy defects, i.e. singly ionized F^+ defects [53]. The PL bands around 470 and 440 nm were seen in SnO_2 nanopowders [54]. These PL bands obtained with similar excitation line as in our case were ascribed to have excitonic origin [54]. It is well known that excitonic bands are formed near the band edge and they are usually of much narrower bandwidth than PL bands which originate from defect structures. As the band gap of the $SnO_{2-\delta}$ sample is around 4 eV, it can be concluded that PL bands at 446 and 470 nm lie deeper in the gap. Hence, it is unlikely that these two bands originate from some excitonic states. Performing density functional calculation for defective $SnO_{2-\delta}$ nanocrystals, Liu *et al.* [38] have shown that PL peaks at 446 and 470 nm originate from the subbridging oxygen vacancies, V_{OSB}. Schematic model for different relaxation processes in the $SnO_{2-\delta}$ nanocrystals is presented in Fig. 7b.

Co-doping induced complete reduction of PL intensity. Even the smallest percent of Co-doping (see Fig. 7a) almost completely quenched the luminescence. By integrating the spectra of the $Sn_{1-x}Co_xO_{2-\delta}$ samples from Fig. 7a, the areas within the boundary of emission were calculated for both undoped and doped samples in order to compare the quantum efficiencies. As the spectra were recorded under the identical excitation/absorption

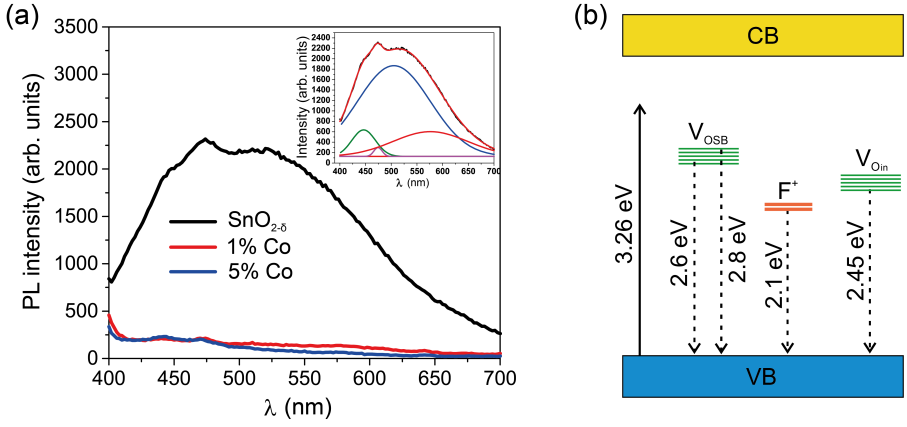

Figure 7. Room-temperature PL spectra of $Sn_{1-x}Co_xO_{2-\delta}$ nanoparticles (a) and the schematic of relaxation mechanism (b)

conditions, the drop in quantum yield value was estimated to be nearly 93%, which evidently implies that cobalt doping drastically quenches the photoluminescence of $SnO_{2-\delta}$. It has been already demonstrated that Co ions act as luminescence quenchers for metal oxides like TiO_2 or ZnO, decreasing the intensity of PL emission by forming the large number of nonradiative centres [55,56]. Therefore, it can be inferred that Co-doping of the $SnO_{2-\delta}$ nanocrystals increases the nonradiative recombination processes.

3.4. Photocatalytic performances

The degradation of MB under the UV light in the presence of the $Sn_{1-x}Co_xO_{2-\delta}$ samples is shown in Fig. 8a. The blank experiment in the absence of the catalyst (black curve) displayed almost no photocatalytic degradation of MB under UV irradiation. The $SnO_{2-\delta}$ nanoparticles exhibited high photocatalytic activity as the degradation of MB was completed after 6 h. The photocatalytic efficiency of the $SnO_{2-\delta}$ nanoparticles is much better than the ones of bulk SnO_2 [53] and is comparable to other reported works on SnO_2 nanoparticles [24,57]. Photoinduced degradation of MB was significantly slower in the presence of Co-doped samples. After 6 h, the MB degradation of 50% was obtained in the presence of the $Sn_{0.99}Co_{0.01}O_{2-\delta}$ catalyst, whereas significant decrease of photocatalytic activity was registered for the $Sn_{0.97}Co_{0.03}O_{2-\delta}$ and $Sn_{0.95}Co_{0.05}O_{2-\delta}$ samples. The obtained results are in accordance with the solitary work of Entradas *et al.* [22] who showed that increased Co-doping resulted in the decreased photocatalytic activity of SnO_2. The experimental kinetic data for $SnO_{2-\delta}$ catalyst were fitted to the rate equation of a pseudo first-order reaction $\ln(C/C_0) = kt$, where k is the rate constant and C_0 and C are the initial dye concentration and that at time t. The reaction kinetics for the $SnO_{2-\delta}$ catalyst (inset of Fig. 8a) follows the first order and the reaction rate constant estimated from the slope of the linear fit is 0.323 h^{-1}. The degradation process of MB is initiated when the electron-hole pairs are formed on the $SnO_{2-\delta}$ surface under the UV irradiation. Photogenerated electrons and holes, if not recombined, can migrate to the catalyst surface and react with adsorbed oxygen, water molecules or hydroxyl anions generating hydroxyl ($OH^\bullet$), superoxide ($O_2^{\bullet-}$) or ($HO_2^\bullet$) radicals. These reactions can be presented by Eq. 4–8:

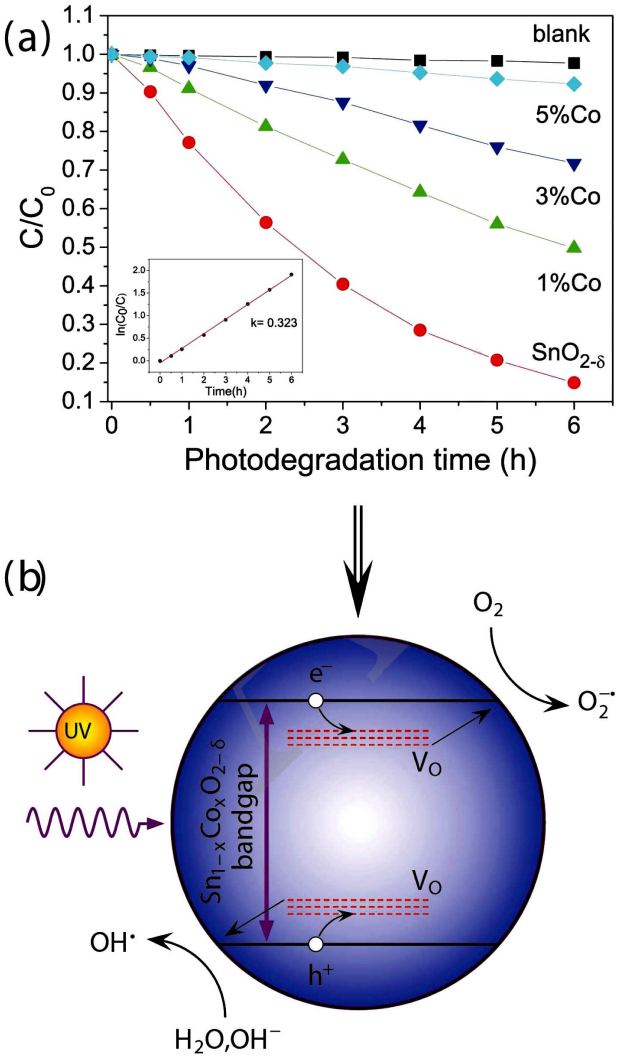

Figure 8. Photocatalytic degradation of MB in the presence of $Sn_{1-x}Co_xO_{2-\delta}$ samples (inset: pseudo first-order reaction kinetics of $SnO_{2-\delta}$ sample) (a) and illustration of proposed photodegradation mechanism under UV light illumination (b)

$$SnO_2 + h\nu \longrightarrow SnO_2(e^-_{cb} + h^+_{vb}) \quad (4)$$

$$e^-_{cb} + O_{2ads} \longrightarrow O_2^{\bullet-} \quad (5)$$

$$h^+_{vb} + H_2O \longrightarrow H^+ + OH^\bullet \quad (6)$$

$$h^+_{vb} + OH^- \longrightarrow OH^\bullet \quad (7)$$

$$O_2^{\bullet-} + H^+ \longrightarrow HO_2^\bullet \quad (8)$$

The photocatalytic efficiency of semiconductors like SnO_2 can be enhanced by introducing lattice defects such as oxygen vacancies because these defects can be active sites on the photocatalyst surface and delay the recombination of photogenerated electrons and holes [21,58]. The as-prepared $SnO_{2-\delta}$ nanopowders are very much oxygen deficient as confirmed by Raman results. The oxygen vacancies can form defect states inside the gap influencing the electronic structure of $SnO_{2-\delta}$ nanoparticles, as already seen from PL spectrum. By applying complementary techniques such as ultraviolet photoelectron spectroscopy and ion-scattering spectroscopy, Cox *et al.* [59] analysed oxygen vacancy electronic states on the SnO_2 surface and they showed that in-plane oxygen vacancies V_{Oin} form defect electronic states inside the SnO_2 gap near the conduction band behaving like F^+ centre donor states. Bridging/subbridging oxygen vacancies form states near the valence band [59] playing the role of hole acceptors. These donor/acceptor states can serve as carrier traps for electrons and holes ensuring better charge separation efficiency and suppression of *e-h* recombination process. Besides, doubly ionized (F^{++}) or singly ionized (F^+)

in-plane or subbridging vacancies formed at the surface of the catalyst facilitate charge transfer to adsorption species like H_2O or O_2, forming reactive radicals responsible for dye degradation. The holes, h^+_{vb}, trapped by oxygen vacancies at the nanoparticle surface react with adsorbed H_2O or OH^- groups to form $OH^\bullet$ radicals (Eqs. 6 and 7). Besides, electrons, e^-_{cb}, can be trapped by surface F^{++} vacancies which convert to F^+. Molecular oxygen adsorbed on the $SnO_{2-\delta}$ surface can capture electrons located on F^+ states [58] to form $O_2^{\bullet-}$ radicals:

$$e^-_{cb} + F^{++} \longrightarrow F^+ \quad (9)$$

$$F^+ + O_2 \longrightarrow O_2^{\bullet-} + F^{++} \quad (10)$$

Therefore, it is reasonable to assume that in-plane and subbridging/bridging oxygen vacancies in different charge states play significant role in enhancing the photocatalytic efficiency of $SnO_{2-\delta}$. The proposed mechanism of photodegradation process is presented in Fig. 8b.

Among the reactive radicals, $OH^\bullet$ radicals are considered to be the most important oxidative agent in photocatalytic reactions on metal-oxide nanostructures. They have one of the highest oxidation potentials among the oxidizing species (2.8 V) and can rapidly attack pollutants on the semiconductor surface. These radicals are considered as non-selective oxidizing species, since they can oxidize almost all electron rich organic molecules because of its electrophilic nature. $OH^\bullet$ radicals are usually formed by the reaction between the holes and OH^- or water molecules present on the surface of the catalyst (Eqs. 6 and 7). The formation of $OH^\bullet$ radicals on the surface of UV-illuminated $SnO_{2-\delta}$ was tested by performing the experiment with terephthalic acid, described in detail in section 2.3. The concentration of $OH^\bullet$ radicals was estimated from the intensity change of the PL peak attributed to 2-hydroxyterephtalic acid which is known to be proportional to the amount of $OH^\bullet$ radicals formed [30,31]. Figure 9 showed that intensity of PL peak at around 430 nm gradually increased with the prolonged irradiation time pointing to the higher formation rate of hydroxyl radicals. This result indicates that increased formation of $OH^\bullet$ radicals has a great effect on the photocatalytic activity of $SnO_{2-\delta}$. Further investigations will be directed to the estimation of the optimal SnO_2 concentration and the influence of solution pH on the SnO_2 photocatalytic properties. In that sense, more detailed mechanism study needs to be performed.

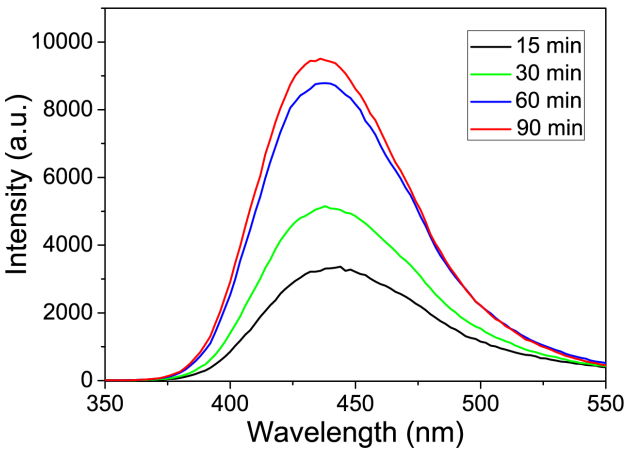

Figure 9. PL intensity change of 430 nm peak observed during UV illumination of $SnO_{2-\delta}$ sample in the solution of terephthalic acid and recorded at different time

With Co-doping the photocatalytic performances of $SnO_{2-\delta}$ were deteriorated. The reasons can be found in increased number of nonradiative centres with increasing cobalt concentration which act as trapping centres, immobilizing the fast transfer of photo-generated electrons to the nanoparticle surface. However, one of the main reasons can be found in the decreased concentration of oxygen vacancies which promotes the charge separation enhancing at the same time the photocatalytic activity. Also, the increased band gap of the Co-doped samples decreases the number of photons with sufficient energy to initiate photocatalytic processes, i.e. less UV energy is absorbed.

IV. Conclusions

Single phase ultrafine $Sn_{1-x}Co_xO_{2-\delta}$ nanocrystals, of a tetragonal (cassiterite-type) crystal structure, were prepared using a simple microwave-assisted hydrothermal synthesis at low temperature without the addition of any surfactant. Rietveld refinement of the XRD data showed that Co cations entered substitutionally into $SnO_{2-\delta}$ lattice and the unit cell volume increased up to $x = 0.05$. The slight shrinkage of the unit cell of the $Sn_{0.95}Co_{0.05}O_{2-\delta}$ sample was ascribed to the increased amount of Co^{3+} cations. The average crystallite size of the $SnO_{2-\delta}$ nanocrystals was less than Bohr exciton radius and it was found to decrease with increasing Co-doping level. UV-Vis absorption measurements confirmed that Co cations entered into the $SnO_{2-\delta}$ lattice in mixed valence state for higher dopant content ($x > 0.01$) and the concentration of Co^{3+} cations increased in the $Sn_{0.95}Co_{0.05}O_{2-\delta}$ sample. Raman spectra revealed oxygen deficient structure of the $SnO_{2-\delta}$ nanocrystals, whereas the oxygen vacancy concentration decreased with increased Co-doping. Further, Co-doping brought significant changes in the optical and electronic properties of tin oxide. $SnO_{2-\delta}$ nanocrystals exhibited blue shift of the band gap energy, compared to the bulk counterpart, due to the combined phonon confinement and the Burstein-Moss effects. The optical band gap energy increased with increasing Co concentration. The luminescence process in $SnO_{2-\delta}$ nanocrystals mainly originated from oxygen vacancy related defects and it was completely quenched in the Co-doped nanocrystals due to the increased nonradiative recombination processes. The oxygen-deficient $SnO_{2-\delta}$ was efficient for the light-induced degradation of methylene blue. Enhanced photocatalytic activity of $SnO_{2-\delta}$ can be ascribed to the

oxygen vacancies-assisted better charge separation and faster charge transport to adsorbed species. On the other hand, deteriorated photocatalytic performances of Co-doped $SnO_{2-\delta}$ nanopowders can be ascribed to the decreased oxygen vacancy concentration and less amount of absorbed UV light because of the band gap widening.

Acknowledgement: The authors acknowledge funding by the Institute of Physics Belgrade, through the grant by the Serbian Ministry of Education, Science and Technological Development. V.D. Araújo and M.I.B. Bernardi wish to thank Brazilian agencies FAPESP, FACEPE and CNPq for financial support.

References

1. H. Park, S. Alhammadi, K. Bouras, G. Schmerber, F. Gérald, D. Aziz, S. Abdelilah, J. Chan-Wook, P. Chinho, K. Woo Kyoung, "Nd-doped SnO_2 and ZnO for application in Cu(InGa)Se_2 solar cells", *Sci. Adv. Mater.*, **9** (2017) 2114–2120.
2. J. Lee, N.H. Kim, Y.S. Park, "Characteristics of SnO_2:Sb films as transparent conductive electrodes of flexible inverted organic solar cells", *J. Nanosci. Nanotechnol.*, **16** (2016) 4973–4977.
3. Y. Chen, J. Lu, S. Wen, L. Lu, J. Xue, "Synthesis of SnO_2/MoS_2 composites with different component ratios and their applications as lithium ion battery anodes", *J. Mater. Chem. A*, **2** (2014) 17857–17866.
4. M. Batzill, U. Diebold, "The surface and materials science of tin oxide", *Prog. Surf. Sci.*, **79** (2005) 47–154.
5. K. Singh, R. Malakar, R. Narzary, K. Priyanka, M. Biplob, "Hydrogen sensing properties of pure and composites of ZnO and SnO_2 particles: Understanding sensing mechanism", *Sens. Lett.*, **15** (2017) 771–778.
6. Z. Zhao, B. Wang, J. Ma, W. Zhan, L. Wang, Y. Guo, Y. Guo, G. Lu, "Catalytic combustion of methane over Pd/SnO_2 catalysts", *Chinese J. Catal.*, **38** (2017) 1322–1329.
7. J.T. Wiswall, M.S. Wooldridge, H.G. Im, "An experimental investigation of catalytic oxidation of propane using temperature controlled Pt, Pd, SnO_2, and 90% SnO_2–10% Pt catalysts", *Catal. Sci. Technol.*, **3** (2013) 618–625.
8. J.S. Chen, X.W.D. Lou, "SnO_2-based nanomaterials: synthesis and application in lithium-Ion batteries", *Small*, **9** (2013) 1877–1893.
9. M.O. Orlandi, A.J. Ramirez, E.R. Leite, E. Longo, "Morphological evolution of tin oxide nanobelts after phase transition", *Cryst. Growth Des.*, **8** (2008) 1067–1072.
10. J. Jeong, S.-P. Choi, C.I. Chang, D.C. Shin, J.S. Park, B.-T. Lee, Y.-J. Park, H.-J. Song, "Photoluminescence properties of SnO_2 thin films grown by thermal CVD", *Solid State Commun.*, **127** (2003) 595–597.
11. Y. Wang, M.H. Wu, Z. Jiao, J.Y. Lee, "One-dimensional SnO_2 nanostructures: facile morphology tuning and lithium storage properties", *Nanotechnology*, **20** (2009) 345704.
12. Z.R. Dai, Z.W. Pan, Z.L. Wang, "Growth and structure evolution of novel tin oxide diskettes", *J. Am. Chem. Soc.*, **124** (2002) 8673–8680.
13. X. Li, Q. Yu, C. Yu, Y. Huang, R. Li, J. Wang, F. Guo, Y. Zhang, S. Gao, L. Zhao, "Zinc-doped SnO_2 nanocrystals as photoanode materials for highly efficient dye-sensitized solar cells", *J. Mater. Chem. A*, **3** (2015) 8076–8082.
14. Y. Liu, F. Yang, X. Yang, "Size-controlled synthesis and characterization of quantum-size SnO_2 nanocrystallites by a solvothermal route", *Colloid Surf. A*, **312** (2008) 219–225.
15. Y.K. Liu, C.L. Zheng, W.Z. Wang, Y.J. Zhan, G.H. Wang, "Production of SnO_2 nanorods by redox reaction", *J. Cryst. Growth*, **233** (2001) 8–12.
16. J.Q. Hu, Y. Bando, Q.L. Liu, D. Golberg, "Laser-ablation growth and optical properties of wide and long single-crystal SnO_2 ribbons", *Adv. Funct. Mater.*, **13** (2003) 493–496.
17. H.Q. Cao, X.Q. Qiu, Y. Liang, L. Zhang, M.J. Zhao, Q.M. Zhu, "Sol-gel template synthesis and photoluminescence of n- and p-type semiconductor oxide nanowires", *Chem. Phys. Chem.*, **7** (2006) 497–501.
18. Y.K. Liu , C.L. Zheng , W.Z. Wang , C.R. Yin , G.H. Wang, "Synthesis and characterization of rutile SnO_2 nanorods", *Adv. Mater.*, **13** (2001) 1883–1887.
19. D. Chen, S. Huang, R. Huang, Q. Zhang, T.-T. Lee, E. Cheng, Z. Hu, Z. Chen, "Highlights on advances in SnO_2 quantum dots: insights into synthesis strategies, modifications and applications", *Mater. Res. Lett.*, **6** (2018) 462–488.
20. P.G. Mendes, M.L. Moreira, S.M. Tebcherani, M.O. Orlandi, J. Andrés, M.S. Li, N. Diaz-Mora. J.A. Varela. E. Longo, "SnO_2 nanocrystals synthesized by microwave-assisted hydrothermal method: towards a relationship between structural and optical properties", *J. Nanopart. Res.*, **14** (2012) 750–13.
21. A.M. Al-Hamdi, U. Rinner, M. Sillanpää, "Tin dioxide as a photocatalyst for water treatment: A review", *Process Saf. Environ.*, **107** (2017) 190–205.
22. T. Entradas, J.F. Cabrita, S. Dalui, M.R. Nunes, O.C. Monteiro, A.J. Silvestre, "Synthesis of sub-5 nm Co-doped SnO_2 nanoparticles and their structural, microstructural, optical and photocatalytic properties", *Mater. Chem. Phys.*, **147** (2014) 563–571.
23. R. Mani, K. Vivekanandan, K. Vallalperuman, "Synthesis of pure and cobalt (Co) doped SnO_2 nanoparticles and its structural, optical and photocatalytic properties", *J. Mater. Sci. Mater. Electron.*, **28** (2017) 4396–4402.
24. D. Chandran, L.S. Nair, S. Balachandran, K. Rajendra Babu, M. Deepa, "Structural, optical, photocatalytic, and antimicrobial activities of cobalt-doped tin oxide nanoparticles", *J. Sol-Gel Sci. Technol.*, **76** (2015) 582–591.
25. Y. Cao, L. Huang, Y. Bai, K. Jermsittiparsert, R. Hosseinzadeh, H. Rasoulnezhad, G. Hosseinzadeh, "Synergic effect of oxygen vacancy defect and shape on the photocatalytic performance of nanostructured TiO_2 coating", *Polyhedron*, **175** (2020) 114214.
26. X. Xu, X. Ding, X. Yang, P. Wang, S. Li, Z. Lu, H. Chen, "Oxygen vacancy boosted photocatalytic decomposition of ciprofloxacin over Bi_2MoO_6: Oxygen vacancy engineering, biotoxicity evaluation and mechanism study", *J. Hazar. Mater.*, **364** (2019) 691–699.
27. Q. Zhang, X. Zhao, L. Duan, H. Shen, R. Liu, "Controlling oxygen vacancies and enhanced visible light photocatalysis of CeO_2/ZnO nanocomposites", *J. Photoch. Photobio. A*, **392** (2020) 112156.
28. B. Matovic, J. Lukovic, B. Stojadinović, S. Aškrabić, A. Zarubica, B. Babic, Z. Dohčević-Mitrović, "Influence of Mg doping on structural, optical and photocatalytic performances of ceria nanopowders", *Process. Appl. Ceram.*,

11 (2017) 304–310.
29. Z. Dohčević-Mitrović, S. Stojadinović, L. Lozzi, S. Aškrabić, M. Rosić, N. Tomić, N. Paunović, S. Lazović, M.G. Nikolić, S. Santucci, "WO_3/TiO_2 composite coatings: Structural, optical and photocatalytic properties", *Mater. Res. Bull.*, **83** (2016) 217–224.
30. T.M. Su, Z.L. Liu, Y. Liang, Z.Z. Qin, J. Liu, Y.Q. Huang, "Preparation of PbYO composite photocatalysts for degradation of methyl orange under visible-light irradiation", *Catal. Comm.*, **18** (2012) 93–97.
31. K. Ishibashi, A. Fujishima, T. Watanabe, K. Hashimoto, "Detection of active oxidative species in TiO_2 photocatalysis using the fluorescence technique", *Electrochem. Commun.*, **2** (2000) 207–210.
32. D. Menzel, A. Awada, H. Dierke, J. Schoenes, F. Ludwig, M. Schilling, "Free-carrier compensation in ferromagnetic ion-implanted SnO_2:Co", *J. Appl. Phys.*, **103** (2008) 07D106.
33. E.J.H. Lee, C. Ribeiro, T.R. Giraldi, E. Longo, E.R. Leite, J.A. Varela, "Photoluminescence in quantum-confined SnO_2 nanocrystals: Evidence of free exciton decay", *Appl. Phys. Lett.*, **84** (2004) 1745–1747.
34. B. Babu, Ch.V. Reddy, J. Shim, R.V.S.S.N. Ravikumar, J. Park, "Effect of cobalt concentration on morphology of Co-doped SnO_2 nanostructures synthesized by solution combustion method", *J. Mater. Sci. Mater. Electron.*, **27** (2016) 5197–5203.
35. P.S. Peercy, B. Morosin, "Pressure and temperature dependences of the Raman-active phonons in SnO_2", *Phys. Rev. B*, **7** (1973) 2779–2786.
36. V. Bonu, A. Das, S. Amirthapandian, S. Dhara, A.K. Tyagi, "Photoluminescence of oxygen vacancies and hydroxyl group surface functionalized SnO_2 nanoparticles", *Phys. Chem. Chem. Phys.*, **17** (2015) 9794–9801.
37. A. Diéguez, A. Romano-Rodríguez, A. Vilà, J.R. Morante, "The complete Raman spectrum of nanometric SnO_2 particles", *J. Appl. Phys.*, **90** (2001) 1550–1557.
38. L.Z. Liu, J.K. Xu, X.L. Wu, T.H. Li, J.C. Shen, P.K. Chu, "Optical identification of oxygen vacancy types in SnO_2 nanocrystals", *Appl. Phys. Lett.*, **102** (2013) 031916.
39. K.N. Yu, Y. Xiong, Y. Liu, C. Xiong, "Microstructural change of nano-SnO_2 grain assemblages with the annealing temperature", *Phys. Rev. B*, **55** (1997) 2666–2671.
40. Y. Liu, M. Liu, "Growth of aligned square-shaped SnO_2 tube arrays", *Adv. Funct. Mater.*, **15** (2005) 57–62.
41. F. Wang, X. Zhou, J. Zhou, T.-K. Sham, Z. Ding, "Observation of single tin dioxide nanoribbons by confocal Raman microspectroscopy", *J. Phys. Chem. C*, **111** (2007) 18839–18843.
42. C. Van Komen, A. Thurber, K.M. Reddy, J. Hays, A. Punnoose, "Structure-magnetic property relationship in transition metal (M = V, Cr, Mn, Fe, Co, Ni) doped SnO_2 nanoparticles", *J. Appl. Phys.*, **103** (2008) 07D141.
43. D.A. Popescu, J.-M. Herrmann, A. Ensuque, F. Bozon-Verduraz, "Nanosized tin dioxide: Spectroscopic (UV-VIS, NIR, EPR) and electrical conductivity studies", *Phys. Chem. Chem. Phys.*, **3** (2001) 2522–2530.
44. I. Rossetti, B. Bonelli, G. Ramis, E. Bahadori, R. Nasi, A. Aronne, S. Esposito, "New insights into the role of the synthesis procedure on the performance of Co-based catalysts for ethanol steam reforming", *Top. Catal.*, **61** (2018) 734–1745.
45. Y. Brik, M. Kacimi, M. Ziyad, F. Bozon-Verduraz, "Titania-supported cobalt and cobalt-phosphorus catalysts: Characterization and performances in ehane oxidative dehydrogenation", *J. Catal.*, **202** (2001) 118–128.
46. S. Roy, A.G. Joshi, S. Chatterjee, A.K. Ghosh, "Local symmetry breaking in SnO_2 nanocrystals with cobalt doping and its effect on optical properties", *Nanoscale*, **10** (2018) 10664–10682.
47. A.S. Ferlauto, G.M. Ferreira, J.M. Pearce, C.R. Wronski, R.W. Collins, X. Deng, G. Ganguly, "Analytical model for the optical functions of amorphous semiconductors from the near-infrared to ultraviolet: Applications in thin film photovoltaics", *J. Appl. Phys.*, **92** (2002) 2424–2436.
48. P.D. Borges, L.M.R. Scolfaro, H.W. Leite Alves, E.F. da Silva Jr., "DFT study of the electronic, vibrational, and optical properties of SnO_2", *Theor. Chem. Acc.*, **126** (2010) 39–44.
49. L. Brus, "Electronic wave functions in semiconductor clusters: experiment and theory", *J. Phys. Chem.*, **90** (1986) 2555–2560.
50. S. Dalui, S. Rout, A.J. Silvestre, G. Lavareda, L.C.J. Pereira, P. Brogueira, O. Conde, "Structural, electrical and magnetic studies of Co:SnO_2 and (Co,Mo):SnO_2 films prepared by pulsed laser deposition", *Appl. Surf. Sci.*, **278** (2013) 127–131.
51. H.S. So, J.-W. Park, D.H. Jung, K.H. Ko, H. Lee, "Optical properties of amorphous and crystalline Sb-doped SnO_2 thin films studied with spectroscopic ellipsometry: Optical gap energy and effective mass", *J. Appl. Phys.*, **118** (2015) 085303.
52. A. Oprea, E. Moretton, N. Bârsan, W.J. Becker, J. Wöllenstein, U. Weimar, "Conduction model of SnO_2 thin films based on conductance and Hall effect measurements", *J. Appl. Phys.*, **100** (2006) 033716.
53. A. Kar, M.A. Stroscio, M. Dutta, J. Kumari, M. Meyyappan, "Growth and properties of tin oxide nanowires and the effect of annealing conditions", *Semicond. Sci. Technol.*, **25** (2010) 024012.
54. I.I. Gontia, M. Baibarac, I. Baltog, "Photoluminescence and Raman studies on tin dioxide powder and tin dioxide/single-walled carbon-nanotube composites", *Phys. Status Solidi B*, **248** (2011) 1494–1498.
55. B. Choudhury, A. Choudhury, "Luminescence characteristics of cobalt doped TiO_2 nanoparticles", *J. Lumin.*, **132** (2012) 178–184.
56. S. Yamamoto, "Photoluminescence quenching in cobalt doped ZnO nanocrystals", *J. Appl. Phys.*, **111** (2012) 094310.
57. S.P. Kim, M.Y. Choi, H.C. Choi, "Photocatalytic activity of SnO_2 nanoparticles in methylene blue degradation", *Mater. Res. Bull.*, **74** (2016) 85–89.
58. X. Pan, M.-Q. Yang, X. Fu, N. Zhang, Y.-J. Xu, "Defective TiO_2 with oxygen vacancies: synthesis, properties and photocatalytic applications", *Nanoscale*, **5** (2013) 3601–3614.
59. D.F. Cox, T.B. Fryberger, S. Semancik, "Oxygen vacancies and defect electronic states on the SnO_2(110)-1 × 1", *Phys. Rev. B*, **38** (1988) 2072–2083.